

# Method and Apparatus for Soft Tissue Material Parameter Estimation Using Tissue Tagged Magnetic Resonance Imaging

**Kevin F. Augenstein<sup>1</sup>**

e-mail: k.augenstein@auckland.ac.nz  
Bioengineering Institute,  
The University of Auckland,  
Private Bag 92019,  
Auckland, New Zealand

**Brett R. Cowan**

Department of Medicine  
The University of Auckland,  
Private Bag 92019,  
Auckland, New Zealand

**Ian J. LeGrice**

**Poul M. F. Nielsen**

**Alistair A. Young**

Bioengineering Institute,  
The University of Auckland,  
Private Bag 92019,  
Auckland, New Zealand

*We describe an experimental method and apparatus for the estimation of constitutive parameters of soft tissue using Magnetic Resonance Imaging (MRI), in particular for the estimation of passive myocardial material properties. MRI tissue tagged images were acquired with simultaneous pressure recordings, while the tissue was cyclically deformed using a custom built reciprocating pump actuator. A continuous three-dimensional (3D) displacement field was reconstructed from the imaged tag motion. Cavity volume changes and local tissue microstructure were determined from phase contrast velocity and diffusion tensor MR images, respectively. The Finite Element Method (FEM) was used to solve the finite elasticity problem and obtain the displacement field that satisfied the applied boundary conditions and a given set of material parameters. The material parameters which best fit the FEM predicted displacements to the displacements reconstructed from the tagged images were found by nonlinear optimization. The equipment and method were validated using inflation of a deformable silicon gel phantom in the shape of a cylindrical annulus. The silicon gel was well described by a neo-Hookean material law with a single material parameter  $C_1 = 8.71 \pm 0.06$  kPa, estimated independently using a rotational shear apparatus. The MRI derived parameter was allowed to vary regionally and was estimated as  $C_1 = 8.80 \pm 0.86$  kPa across the model. Preliminary results from the passive inflation of an isolated arrested pig heart are also presented, demonstrating the feasibility of the apparatus and method for isolated heart preparations. FEM based models can therefore estimate constitutive parameters accurately and reliably from MRI tagging data. [DOI: 10.1115/1.1835360]*

*Keywords:* MRI, Constitutive Estimation, Passive Cardiac Mechanics, Diffusion Imaging, MRI Tagging, Finite Element Modeling

## Introduction

The stiffness or compliance of soft tissue organs can substantially influence their function, and alterations in tissue material properties are often indicative of disease processes. Estimates of soft tissue material properties are therefore very important in the evaluation of the type or degree of pathology, or the potential response to treatment. One major area of interest is the diastolic function of the heart. Diastolic dysfunction is commonly observed in heart failure patients, and may occur before measurable evidence of systolic dysfunction [1]. Factors influencing diastolic function include preload (filling pressure), afterload (wall stress), and the passive material properties of myocardium. Stiffening of the left ventricular myocardium leads to the impairment of filling, which in turn results in increased ventricular filling pressure, increased cardiac work, and decreased pump function. Thus, changes in the diastolic material properties of the myocardium in disease may be useful clinical indices of disease progress and may enable the quantification of treatment benefit.

Previously, uniaxial and biaxial material tests have been employed to characterize the material behavior of soft tissues [2,3]. However, these techniques often involve sectioning the tissue, which introduces problems associated with the disruption of the microstructure, and the maintenance of tissue homeostasis [4]. In

addition, these tests may not incorporate all the modes of deformation experienced in-vivo, and are usually too invasive for clinical use.

Since it is not possible to estimate myocardial stiffness directly and noninvasively, surrogate measures of compliance and function are used clinically. These have included pressure volume loops recorded by a conductance catheter, and the left ventricle (LV) filling rate, wall thickening and wall motion using the tissue strain rate from tissue Doppler or strain rate echocardiography. The latter is becoming common in the clinical domain because it is relatively inexpensive and noninvasive; however, velocities and strain rates can only be recorded along the axis of the ultrasonic transducer.

A powerful alternative technique is MRI with tissue tagging [5,6]. In one method, known as SPAtial Modulation of Magnetization (SPAMM) [6], a series of saturation tags are created within the heart immediately after the electrocardiogram (ECG) R-wave, using a short pulse of nonselective radio frequency bursts separated by field gradients. The tags move with the myocardium as it deforms through the cardiac cycle, and appear as a set of dark stripes on the resulting images. Images are typically acquired over several heartbeats; the tags are reapplied at each R-wave and fade with the longitudinal relaxation time constant (T1, approximately 800 ms for myocardium at 1.5 Tesla). Image tags can be tracked from frame to frame in multiple slices and used to reconstruct the 3D deformation field [7].

MRI can also be used to probe the tissue microstructure, using MR diffusion tensor imaging [8,9]. This technique quantifies the molecular diffusion of water molecules within the tissue. Cellular membranes, organelles, larger molecules, and various compart-

<sup>1</sup>Corresponding author.

Contributed by the Bioengineering Division for publication in the JOURNAL OF BIOMECHANICAL ENGINEERING. Manuscript received by the Bioengineering Division October 22, 2003; revision received August 31, 2004. Associate Editor: Jay D. Humphrey.

ments within the tissue disrupt the free diffusion of water, and the preferential direction of diffusion can provide structural information on the biological tissue. In anisotropic tissue, diffusion is characterized by a symmetric second order tensor, the eigenvectors of which give the principal directions of the tissue structure. This technique has been used to study the anisotropy inherent in the brain, spinal column, skeletal muscle, and myocardium [8,10–12].

The estimation of material properties requires knowledge of the stress field as well as the strain field. Unfortunately, no technique currently exists for the direct measurement of stress in the heart wall. However, given knowledge of the loading or boundary conditions acting on a soft tissue structure, together with the geometry and material properties, it is possible to use the finite element (FE) method [13] to solve the resulting equations of motion and estimate deformation and stress. Realistic FE models of the whole heart have been developed [14–16] which accommodate the complex 3D geometry and microstructure, large deformations and nonlinear orthotropic material laws governing myocardial tissue behavior. These FE solutions can therefore be incorporated into a material parameter estimation procedure in which the predicted solution is optimized to the experimentally measured geometry, deformation field, and applied boundary conditions.

We describe a method and apparatus for the determination of the passive material properties of soft tissue structures, such as the heart, using MRI tissue tagging. Cyclical deformation of the structure was performed using a custom built reciprocating pump actuator under microprocessor control. Gated SPAMM tagged MRI images were acquired, while the applied loads were recorded. The 3D deformation field was reconstructed from the image tags as described previously [17,18]. The optimal material parameters were found by matching the recorded boundary pressures and imaged 3D deformation to the FE solution of a nonlinear, large-deformation, finite elasticity problem. The validation of the apparatus and parameter optimization method was performed using a deformable silicon gel phantom in the shape of a cylindrical annulus. The material parameters of the gel estimated from the FE optimization procedure were compared with independent material testing. The feasibility of the apparatus in the case of an isolated arrested porcine heart was also demonstrated.

## Materials and Methods

**Apparatus.** In developing an apparatus for the estimation of soft tissue material properties from MRI data, we were influenced by the following design requirements:

- i. Various loading patterns (flow profiles and volumes) must be possible.
- ii. Many deformation cycles are required to build up each tagged MR image series, using gated image acquisition, with a high degree of reproducibility between cycles.
- iii. A cycle frequency of at least 0.5 Hz is required to image the complete deformation, since MR tags fade according to the T1 exponential time constant (i.e. tag contrast reduces to 14% of initial contrast after two T1 periods).
- iv. The scanner must be triggered so that tagging and imaging are performed in synchrony with the deformation.
- v. MR image artifacts must be avoided (e.g. no metal in the imaging area, and no radio frequency sources or electromagnetic equipment are allowed in the scanner room).
- vi. Force boundary conditions must be recorded in a manner that is not susceptible to the rapidly switched magnetic field gradients generated by the scanner.
- vii. Physiological loading conditions and deformations must be applied (in the case of the passive inflation of an isolated pig heart, the stroke volume must be up to 100 mL with a maximum filling pressure of 6 kPa).

Figure 1 shows a schematic of the system. A reciprocating pump was built to inflate the heart cyclically with physiological

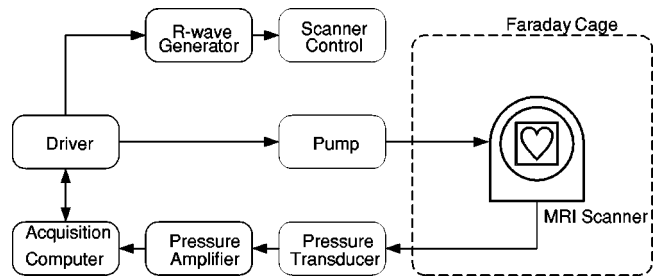


**Fig. 1** A schematic showing the design of the apparatus used for both the gel and isolated heart inflation experiments. All electrical equipment was required to be outside the scanner room. Open loop control was used to control the piston pump. A TTL pulse was sent from the control unit at the commencement of each cycle. This pulse was converted to a triangle pulse to trigger the scanner image acquisition.

saline. Due to its metallic and electromagnetic components, the pump was positioned outside the scanner room and was therefore separated from the heart by five meters of braided tubing with an outer diameter of 18 mm and an inner diameter of 12 mm.

The cylinder of the reciprocating pump (100 cm long, 10 cm inner diameter) was made of anodized-aluminum, treated to enable the use of saline. The piston was driven via a lead screw (pitch 6.3 revolutions/cm) by a stepper motor (LH2318T-M300R10, Eastern Air Devices) and driver (D106CH, Eastern Air Devices) capable of a maximum stepping rate of 30 kHz with a stalling force of 620 N (corresponding to a maximum pressure of 79.3 kPa and a maximum flow rate of  $1.86 \text{ L s}^{-1}$ ). Stepper motor pulse generation was provided by a microprocessor (A-Engine-86-P, Tern) programmable in C, allowing the generation of near-arbitrary pulse sequences and movement profiles. The microprocessor code was downloadable from a PC using a standard serial port connection and custom written software.

The microprocessor was also programmed to generate Transistor–Transistor Logic (TTL) pulses to signal the beginning of a cycle. This trigger pulse was used to generate a triangular pulse 20 mV high and 30 ms long to simulate an ECG R-wave. This trigger signal was input into a scanner ECG detection system and used to trigger the image acquisition.

A variety of piston motion profiles were implemented, including sinusoidal, parabolic, trapezoidal, and sawtooth motions. In practice, the ability of the stepper motor actuator to perform a given motion was limited by the maximum acceleration, since the major component of the force experienced by the piston was due to acceleration of the fluid in the piston and hose. A parabolic motion profile was therefore employed to give the maximum stroke for a given maximum acceleration and cycle frequency, since the acceleration in this case is constant in magnitude and changes sign twice per cycle.

A diaphragm pressure transducer (P23 GOULD Statham) connected to a fluid filled catheter 6 m in length recorded the pressure in the ventricle. The frequency response of the pressure transducer and catheter system was determined by recording the step response to a sudden change in pressure. The response was found to be flat with minimal lag to 30 Hz, above which appreciable lag and attenuation were observed. Since the system was used with cycle rates of less than 1 Hz, frequencies above 30 Hz were filtered from the pressure signal during acquisition. An analog line on a data acquisition card (DAQCARD-1200 National Instruments) was used to acquire the pressure signal at 300 Hz. A counter recorded the number of gating signals sent.

The control software was written in Tcl/Tk 8.2 and the acquisition software was written in LabVIEW (LabVIEW 6i, National Instruments). Data acquisition card and microprocessor control lines were driven by a 233 MHz laptop computer (Acer Computers).

**Gel Phantom.** A silicon gel (Sylgard 527, Dow Corning) deformable MR phantom was cast in the shape of a cylindrical annulus. This gel has similar magnetic relaxation time constants (T1 and T2) to heart muscle, and has previously been used to validate reconstruction of 3D deformation and strain from MR tagged images [19]. In addition, this gel can reproduce a range of material stiffnesses and has been used to validate a device for measuring soft tissue shear behavior [4]. The MR phantom had an outer diameter of 100 mm, an inner diameter of 45 mm, and a height of 85 mm. The two end faces were fixed by attachment to top and bottom plates with silicon sealant, while the cylindrical inner and outer boundaries of the phantom were free to deform with no surface tractions.

The gel components (453 g of resin and 226.5 g of catalyst) were mixed using a magnetic stirrer for 17 minutes, placed in a sealed chamber, and degassed with a vacuum water pump to remove air bubbles. The mixture was then poured slowly into the annular mold. In addition, some of the same mixture was poured into a smaller cylindrical annulus mold (16 mm inner diameter, 38 mm outer diameter, and 24 mm height) for independent rotational shear testing. All samples were cured at 40°C for 16 hours.

**Gel Material Testing.** In order to provide an independent measure of the material properties of the silicon gel used in the construction of the MR phantom, a rotational shear test was performed using the smaller cylindrical annulus, as described by Dokos et al. [4]. After curing, the end faces of the shear test annulus mould were carefully removed, leaving the inner and outer mold cylinders bonded to the inner and outer gel diameters. The test annulus was then mounted in a rotational shear device, which fixed the inner cylinder and allowed the outer cylinder to rotate freely. Various loads were applied to the outer cylinder to induce rotation via two parallel strings attached horizontally in grooves inscribed on the outer cylinder. Material markers consisting of fine particles of graphite were placed on the topmost surface of the gel and imaged using a high-resolution camera (Camelia 4M, ATMEL). Individual particles were manually tracked and their center of mass was used to calculate the deformation. An incompressible neo-Hookean strain energy function has previously been found to give good approximations to extension and shear tests of the silicon gel [4]. Assuming this form of material law, the analytic solution to the rotational shear test is given by

$$\frac{\omega}{F} C_1 = \frac{A(a^{-2} - R^{-2})}{4\pi h} \quad (1)$$

where  $\omega$  is the angular rotation of a particular material point,  $F$  is the force applied to the outer cylinder,  $A$  and  $a$  are the outer and inner radii of the annulus,  $R$  is the radial position of the material point,  $h$  is the height of the annulus, and  $C_1$  is the neo-Hookean material constant. The material parameter was estimated by performing a linear least squares fit of the above equation to the imaged material marker positions and displacements.

**Isolated Heart Preparation.** A 22 kg pig was initially anaesthetized with zoletil and then maintained with 2.5% halothane in oxygen. The right femoral artery was cannulated to monitor arterial pressure and a pigtail catheter was inserted into the left ventricle via the right carotid artery. A median and left lateral thoracotomy was performed to expose the heart. The left main coronary artery and right coronary artery were dissected near their origins and ties loosely placed for coronary occlusion after arrest. The animal was heparinized (100 IU/kg) via the right carotid artery catheter. A snare was placed around the aorta and the heart was arrested by injection of cold potassium citrate (60 mL, 15%) into the left ventricle via the catheter, while simultaneously tightening the aortic snare, thereby perfusing the heart with potassium citrate via the coronary arteries and causing immediate arrest in a relaxed state. The heart was then rapidly removed and rinsed in cold saline, before being perfused with 2,3-butanedione monoaxime (2,3-BDM) (200 mL, 50 mM in saline) through cannulae inserted into

the right and left coronary ostia. The coronary arteries were then occluded using the previously placed snares to stop any subsequent flow through the aorta entering the coronary network.

A slit was made in the left atrium to allow access to the mitral valve. A large-bore cannula with an annular disk on the end was introduced through the mitral valve, and a thread looped around the cordae tendineae, and tied tight to the cannula above the disk. A second disk was then screwed down on to the valve leaflets clamping them between the upper and lower disks and forming a seal. The aortic valve was made incompetent by incising the leaflets and a large diameter cannula introduced in the aorta and sealed with a snare about the aorta. The heart was placed in a Plexiglas box (160×160×160 mm) with cannula protruding through holes in the lid and filled with chilled saline.

**Image Acquisition.** MR imaging was performed using a standard clinical MRI scanner (Siemens Symphony 1.5 Tesla MRI with a maximum gradient amplitude of 25 mT/m and a slew rate of 42 T/m/s). The Plexiglas container was filled with physiological saline solution and was clamped into a standard head coil. The mitral cannula was attached to the reciprocating pump tube and the aortic cannula attached to the pressure line. Standard axial, coronal, and sagittal scouts were obtained (thickness 3.0 mm, spacing 3.0 mm, 32 slices, field of view (FOV) 135×180 mm for the heart and 200×200 mm for the phantom) spanning the region of interest.

**Deformation Imaging.** SPAMM tagged images were acquired (FOV 200×200 mm, 6 mm slice thickness, 5 deg flip angle, 128×256 matrix, 16 phases, and 5 mm stripe spacing in a grid pattern) at six short axis positions, and at thirty-degree increments about the central axis of the left-ventricle or phantom. A segmented  $k$ -space gradient-echo turboFLASH imaging sequence was used (seven lines per segment, repetition time TR=188 ms, echo time TE=4 ms, 2 averages), requiring 38 deformation cycles per image slice to acquire. In addition, anatomical untagged gradient echo images were acquired (five lines per segment, TR=176 ms, TE=4.8 ms, no averages) in order to determine the geometry of the heart.

**Flow Imaging.** In order to obtain an independent measure of the ventricular or phantom inflow and outflow during the deformation cycle, phase contrast velocity MR images were acquired at the level of the mitral inlet (FOV 150×150 mm, 5 mm slice thickness, 256×256 matrix, 64 phases), gated on every alternate R-wave so that the entire cycle was acquired. These allowed the calculation of volume inflow and outflow through the mitral annula throughout the deformation cycle.

**Diffusion Tensor Imaging.** After the deformation experiments, diffusion tensor imaging was performed with the heart at zero transmural pressure, in order to obtain information on the tissue microstructure. A pulsed gradient spin echo diffusion sequence with echo planar imaging and slice readout (2D multislice acquisition, 12 contiguous axial slices, 5 mm slice thickness, TR/TE 14589.0/100.06 ms, no averages) was modified to acquire diffusion-weighted images as described by Bassler and Pierpaoli [9]. Six diffusion gradient direction images (along with a zero-weighted image) were acquired per slice, with diffusion weighting (b) values of 500, 1000, 1500, and 2000 s/mm<sup>2</sup> in each direction, resulting in a data set of 28 images per slice. These were used to estimate the six independent components of the diffusion tensor as described below.

**Image Data Analysis.** Contours marking the inner and outer boundaries of the gel phantom were delineated by hand on each image separately using the Spammvu software package [20]. The boundaries of the heart were determined from the untagged images using guide point modeling [21]. In this procedure a 3D FE model of the left ventricle was interactively fitted to the imaged boundaries. The model was then imposed on the tagged images to

provide inner and outer boundaries, using the registered positions of the images. Tags were tracked throughout the cycle using custom written software that implements an active contour method for semi-automated tag tracking [7].

The 3D displacement was reconstructed from the tracked image tags using previously described and validated methods [17,19]. Initially (in the first frame, shortly after tag creation) the tags are straight and orthogonal to the image planes. Each stripe point in each subsequent (deformed) frame therefore provides a one-dimensional constraint on the displacement back to the initial frame: i.e. the displacement orthogonal to the original tag plane is known but the displacements parallel to the tag plane are not. Taken together, the orthogonal tag planes then provide a full 3D set of displacements. A FE model was fitted to the inner and outer boundaries in each deformed frame, and the displacement to the initial frame was fitted to the tracked image tag displacements. Since the tags only track motion perpendicular to the tagging plane, the following error function was minimized to reconstruct the initial configuration:

$$E(\mathbf{x}) = S(\mathbf{x}) + \sum_t \{ \mathbf{n}_{T(t)} \cdot [\mathbf{x}(\xi_t) - \mathbf{x}_t] \}^2, \quad (2)$$

where  $E(\mathbf{x})$  is the error,  $S(\mathbf{x})$  is a Sobolov smoothing matrix used to regularize the problem in regions of low data [7],  $\mathbf{n}$  is the unit vector perpendicular to the tagging plane  $T$  associated with data point  $t$ ,  $\mathbf{x}(\xi_t)$  is the model embedded data point, and  $\mathbf{x}_t$  is the tracked tag point. This process effectively reconstructs the 3D motion of the material points on the tag stripes.

Flow encoded phase images were masked by applying a threshold to the magnitude component images, and the velocity (phase component) images were then integrated over the area of the in-flow pipe to obtain the flow rate. Flow rates were then numerically integrated over time to obtain the flow (stroke volume) profile.

The 3D diffusivity tensor was calculated using a modified version of the method outlined by Bassar and Pierpaoli [9]. Since multiple  $b$  values had been acquired, a plot of  $\ln(A/A_0)$  vs  $b$  ( $A$  and  $A_0$  being the signal value in the diffusion weighted image and the signal value in the zero-weighted image, respectively) should be linear, with the slope related to the diffusivity in the gradient direction. Therefore, slopes of this relation were found for all six directions and the following equations solved for the six independent components of the diffusivity tensor:

$$s_i = -2\mathbf{r}_i^T \mathbf{D} \mathbf{r}_i \quad (3)$$

where  $s_i$  is the slope of the  $\ln(A_i/A_0)$  relationship,  $\mathbf{r}_i$  is the  $i$ th diffusion direction, and  $\mathbf{D}$  is the diffusivity tensor. The dominant diffusion direction is given by the eigenvector associated with the largest eigenvalue of the diffusion tensor. In the heart, this corresponds to the mean muscle fiber direction in the imaged voxel [10–12].

**The Mathematical Model.** The motions and stresses within a deformable object can be found using the Finite Element Method (FEM) to solve the equations of motion arising from the theory of finite elasticity [13,16].

In the case of the silicon gel phantom, material tests have shown that the neo-Hookean material law gives acceptable agreement between theoretical and experimental behavior [4]. This law has a single material constant in the strain energy function:

$$W = C_1(I_1 - 3) \quad (4)$$

In the case of myocardium, various transversely isotropic and orthotropic nonlinear strain energy functions have been proposed. Examples include a Fung exponential transversely isotropic law [22–24] and an orthotropic “pole-zero” law [25–27], which is based on the laminar architecture of the heart. Recently, Criscione et al. [28] have shown that myocardial material laws written as a function of principal invariants are fundamentally ill-posed in terms of estimating material parameters. Since the current study is

concerned with methodology and apparatus, we leave the in-depth characterization and estimation of particular myocardial material laws to future studies. An initial attempt at estimating material parameters is presented to demonstrate the feasibility of the method, using the transversely-isotropic Fung-type exponential as used previously by Guccione [23] and shown below:

$$W = \frac{1}{2} C (e^{b_1 e_{ff}^2 + b_2 (e_{rr}^2 + e_{ss}^2 + 2e_{sr}e_{rs}) + 2b_3 (e_{fs}e_{sf} + e_{fr}e_{rf})} - 1) \quad (5)$$

where  $C_1$ ,  $b_1$ ,  $b_2$ , and  $b_3$  are material constants and  $e_{ij}$  are components of the Lagrangian strain tensor  $E$  referred to the local fibre ( $f$ ), transmural or radial ( $r$ ) and cross-fiber ( $s$ ) coordinates. This material law implies material symmetry about the muscle fiber direction,  $f$ , which is defined in the FE model using the fitted fibers from the diffusion tensor MRI.

In the case of the isolated arrested heart, the boundary conditions are the LV cavity pressure and the attachment of the mitral and aortic cannulae. In the gel phantom, the boundary conditions are the applied pressure and the fixed ends. Both the gel phantom and heart were suspended in physiological saline to remove body forces.

The finite elasticity equations were solved with the Galerkin finite element method, using isoparametric tri-cubic Hermite 8-node elements [16], in the CMISS FEM package [29], a custom software program developed specifically for use with high order basis functions and finite deformation elasticity. A cylindrical annulus FE model was custom built to characterize the deformable silicon gel phantom. A variety of mesh resolutions were considered to determine the level of mesh refinement required to obtain a converged solution to the finite elasticity problem. The deformation profiles of each mesh were compared in a simulated deformation of 6 kPa applied internal pressure load and neo-Hookean parameter of 6.5 kPa, in order to test for convergence of the FE model stress solution.

**Estimation of Material Properties.** The basic estimation algorithm was as follows:

1. Determine the reference (no load) geometry, and initial estimates for material parameters.
2. Use the FE model with measured boundary conditions to solve the finite elasticity problem and predict deformed geometry and stress.
3. Compare model deformation with 3D deformation reconstructed from the imaged tags.
4. If the objective function is too large, adjust material parameters and repeat steps 2–3.

The objective function was defined to be:

$$e = \sum_{i=1}^N \|\mathbf{x}_i - \mathbf{x}(\xi_i; \mathbf{C})\|_2^2 \quad (6)$$

where  $N$  is the number of reconstructed data points,  $\mathbf{x}$  is the deformed data point within the sample, and  $\mathbf{x}(\xi; \mathbf{C})$  is the predicted location of the data point in the deformed mesh, obtained using the material parameters  $\mathbf{C}$ . The material parameters were assumed constant within each element of the model, but in general could vary from element to element.

The sequential quadratic programming (SQP) optimization technique was used to adjust the material parameters in order to minimize the objective function [30]. Briefly, SQP involves the solution of a quadratic problem with linearized constraints at each step in the optimization process. This has an analytic solution and can be solved directly. In addition, it then performs a line search to find an improved position. The Hessian is approximated using the local gradient, as is common for sums of squares problems. The SQP method requires the evaluation of derivatives of the objective function with respect to the optimization variables (the material parameters). These derivatives were not available analyti-

cally and so were computed using finite difference estimation. Initial estimates of the material parameters for the gel were taken from previous shear experiments [4] and published estimates from a cylindrical approximation for canine myocardium were used for initial estimates of parameters for the porcine myocardium ( $C_1 = 1.2$ ,  $b_1 = 26.7$ ,  $b_2 = 2.0$ , and  $b_3 = 14.7$ ) [23]. Constraints on the material parameters were placed to ensure they remain within limits (for the neo-Hookean case the bounds were  $1.0 < C_1 < 15.0$  kPa).

For each optimization iteration, a series of finite elasticity problems must be solved: one for the current solution and one for each finite difference derivative approximation. For each of these FE solutions the solver is started from the previous solution. The finite elasticity code allowed the calculation of the individual element stiffness matrices to be performed in parallel on separate processors. A combined relative and absolute tolerance of 0.001 of the L2 norm of the change in the material parameters was used as the convergence criterion for the optimization.

**Sensitivity of Estimated Parameters to Tag Data.** Monte Carlo simulations were performed to estimate the degree to which noise in the input data (i.e. the tracked 3D material displacements of the imaged points) affects the estimated material parameters. The models used for the simulations were the same as those used for the estimation of material properties from the MR images. Material parameters were chosen to be the values estimated from the MR images. The finite elasticity problem was then solved for the same applied pressure loading. From this model, simulated 3D tag displacement data were generated using the same tag resolution as in the MR experiments. Normally distributed noise was then added to the 3D displacement data at various levels. Since the root mean squared (RMS) error in 3D tag displacement reconstruction is typically close to the image pixel size [19,31,32], the simulations were performed using normally distributed zero mean noise with standard deviations of 0.4, 0.8 (approximately equal to the image pixel size), 1.6, and 3.2 mm.

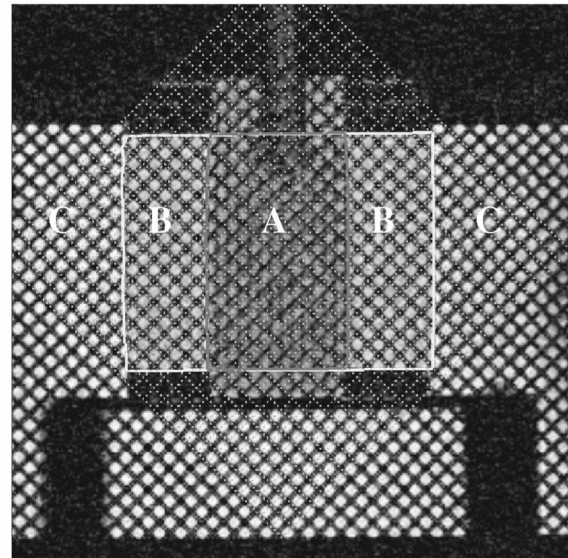
The simulated 3D data point displacements were then used in the parameter estimation procedure to calculate the material parameters. This was repeated 10 times for each noise level and number of frames to estimate the variance in the fitted material parameters.

## Results

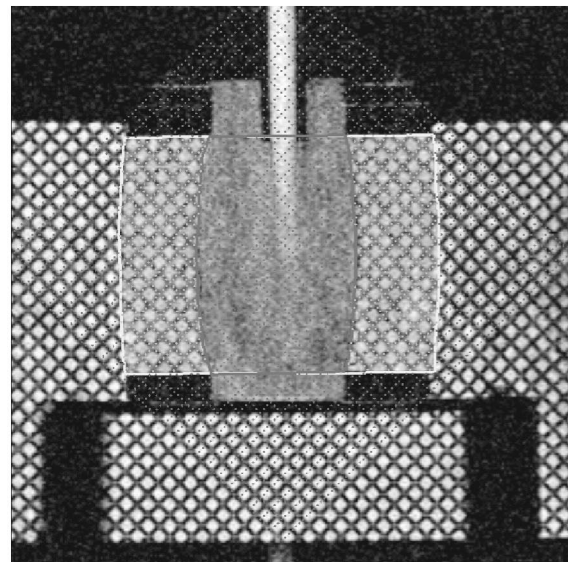
**Gel Phantom.** The gel phantom was imaged while undergoing an inflation/deflation cycle with a period of 1.2 s in which the piston position was controlled in a parabolic motion profile with a stroke volume of 40 mL. The range of pressures recorded was approximately 0–3.1 kPa. The pressure recording was averaged into bins corresponding to each frame in the MR image sequence. Examples of SPAMM tagged images at tag creation and at the frame corresponding to maximum internal pressure are shown in Fig. 2. Due to compliance in the 6 m length tube, the flow profile and stroke volume were somewhat different at the gel than at the piston.

Several refinements of mesh resolution were constructed to obtain a converged FE solution to the gel phantom deformation. Tri-cubic Hermite basis functions were used to describe geometry and deformation with  $C^1$  continuity between elements. A tri-linear basis function was used to describe the hydrostatic pressure within each element. The convergence of the FE solution is illustrated in Fig. 3, which shows the displacement in the outward direction of points on a radial line going from inner to outer surfaces in the equatorial plane. It can be seen that a model consisting of one element transmurally, four elements longitudinally and eight elements circumferentially was sufficient to describe the deformation, with further refinements giving the same profile.

A neo-Hookean material law was assumed with the material parameter constrained to be constant within each element, but allowed to vary between elements. The same 32-element model



(a)



(b)

**Fig. 2 Typical axial SPAMM tagged images showing inflation of the deformable silicon gel phantom. The long axis of the phantom is aligned vertically in the image. Region A is water inside the inner cavity, region B is the silicon gel annulus, and region C is water outside the gel phantom. Note tag fading in the gel relative to free water outside the gel, due to the shorter gel T1 relaxation time constant. Dark and light lines denote inner and outer boundaries, respectively, and points denote tracked tag saturation stripes. (a) Zero relative internal pressure; (b) 3.1 kPa relative internal pressure.**

was used in the tag reconstruction process and the parameter estimation procedure. Parameter estimation required seven iterations to converge and took approximately 2 hours to run on an IBM Regatta using eight Power4 processors. The parameters averaged 8.80 kPa, with a standard deviation of 0.86 kPa, over all elements. The FE model is shown in relation to the SPAMM tagged images, together with the resulting circumferential extension ratio in Fig. 4.

A simpler problem with a constant material parameter throughout the model was also solved, and the optimum material parameter was 8.91 kPa.

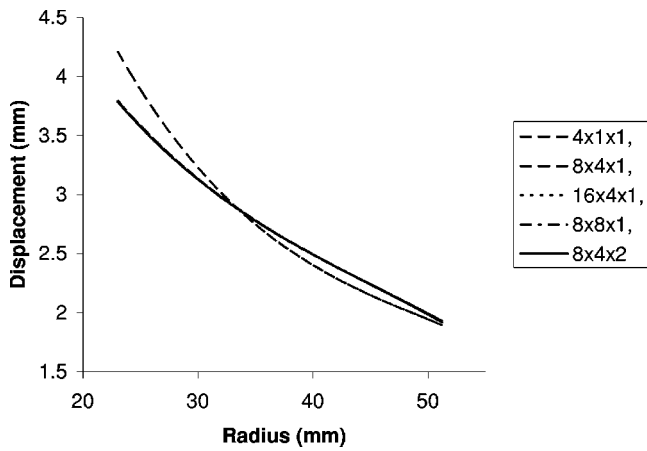


**Fig. 3** Radial displacement profile at the centerline with various mesh resolutions for the cylindrical gel phantom model. The legend refers to the number of elements in the circumferential, longitudinal, and radial directions, respectively. All models overlie the 8×4×1 model, except the 4×1×1 model.

**Rotational Shear Testing Validation.** The rotational shear test specimen and material markers are shown in Fig. 5(a). The tracked displacements of 15 markers on the top surface of the rotational shear test specimen at four different load states were used to estimate the material parameter  $C_1$  in Eq. (1) by linear least squares. Figure 5(b) shows a plot of the resulting left and right hand side terms in Eq. (1) and the line of best fit. The estimated material parameter was  $C_1 = 8.71 \pm 0.06$  kPa (slope  $\pm$  std. error of the estimated slope).

**Confidence Limits on Estimated Parameters.** Using the fitted parameters, we simulate synthetic data sets by adding normally distributed random noise to the data set. The method is applied to each of the synthetic data sets and a set of parameters estimated; by computing the variance in these parameter sets, we can create confidence intervals that are valid for the modeled er-

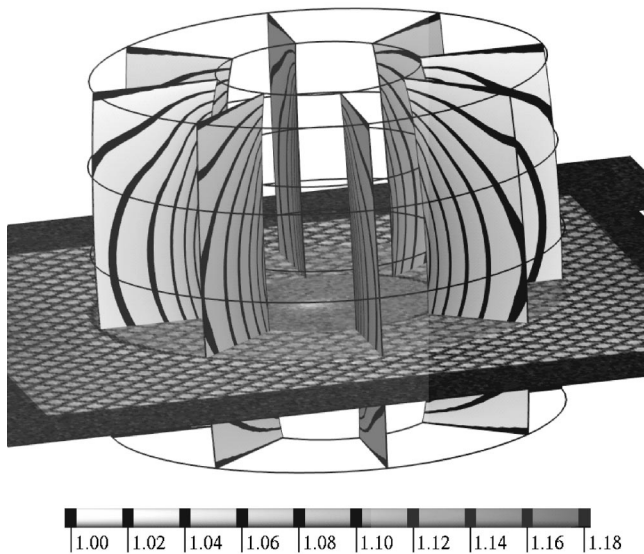


**Fig. 4** SPAMM tagged image and gel phantom finite element model. The color map shows the circumferential extension ratio, while lines show boundaries of the phantom model.

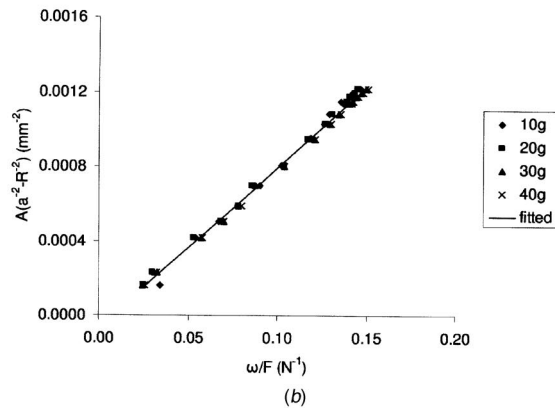
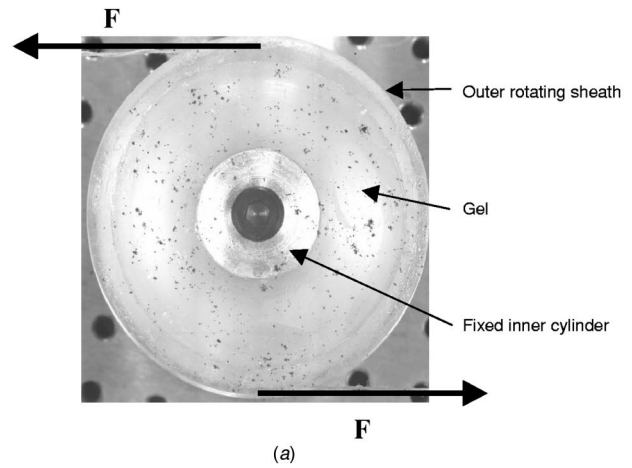


**Fig. 5** (a) Plan view of the rotational shear test apparatus. Moment couple  $F$  is applied to the outer cylinder, which is free to rotate with respect to the inner (fixed) cylinder. (b) Rotational shear test results for four different loading states and 15 radial positions. The plot shows the normalized data and fitted curve (slope  $C_1 = 8.72$  kPa;  $R^2 = 0.9974$ ).

ror. Ten Monte Carlo simulations of the parameter estimation procedure were then performed, with normally distributed zero mean, 0.8 mm std. dev. noise added to the tag displacement data. Using a single material parameter across the whole model, a 95% confidence interval for the estimated material parameter was (8.81, 8.99). In the case of a spatially varying material parameter which was allowed to vary over the 32 elements of the model, the average 95% confidence interval was (8.49, 9.08).

**Isolated Heart Tests.** The isolated arrested heart was imaged while undergoing an inflation/deflation cycle of period 1.2 s in which the piston was controlled in a parabolic motion profile with a stroke volume of 16 ml. The range of pressures recorded was 0–2 kPa. Sample long and short-axis SPAMM tagged images in the initial and maximum pressure frames are shown in Fig. 6. Mitral flow was calculated from the phase contrast MR velocity images and Fig. 7 shows the resulting pressure–volume relationship. A nonlinear compliance is evident, together with hysteresis due the viscoelastic effects, which is commonly observed in isolated heart experiments.

Figure 8 shows the fiber field estimated for the diffusion weighted images. Initial FE estimated material parameters used a spatially constant Fung-type exponential law, with four material parameters. The fitted parameters, from Eq. (5) fitted, were  $C = 3.00$ ,  $b_1 = 11.09$ ,  $b_2 = 1.76$ , and  $b_3 = 10.00$ . This corresponded to a RMS error of 0.24 mm per data point. The correlation between the fitted parameters was significant, with  $b_2$  and  $b_3$  having a correlation of 0.83, indicating that these parameters are coupled

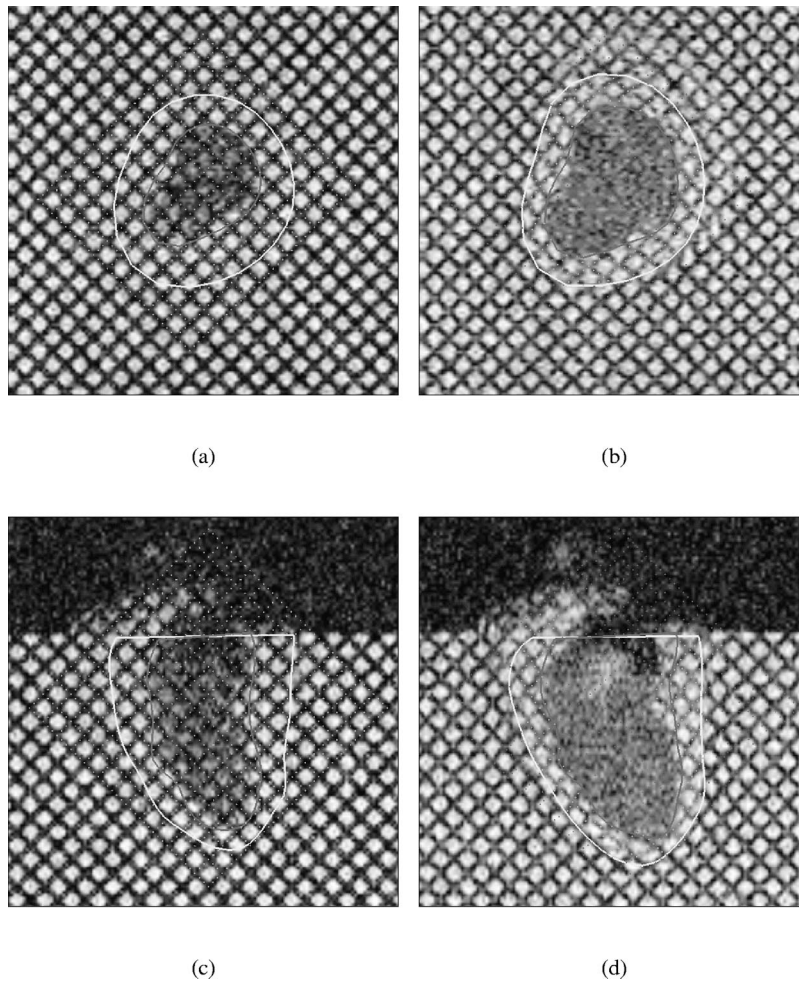


**Fig. 6 Tagged MRI from the isolated heart passive inflation. Dark lines denote endocardial myocardial LV boundaries and light lines denote epicardial LV boundaries. Points denote tracked tag stripe points. (a) Short axis 0 kPa; (b) short axis 1.5 kPa, (c) long axis 0 kPa; (d) long axis 1.5 kPa.**

and may not be accurately determined by the data. However, these parameters were similar in magnitude to those reported previously by Guccione et al. [23] from the passive inflation of isolated arrested dog hearts ( $C_1=1.2$ ,  $b_1=26.7$ ,  $b_2=2.0$ , and  $b_3=14.7$ .)

Monte-Carlo simulations around these parameters were performed at RMS noise levels of 0.4, 0.8, 1.6, and 3.2 mm. In the estimation procedure, we included one, three, or five frames of the MR sequence in the optimization procedure. The standard deviation

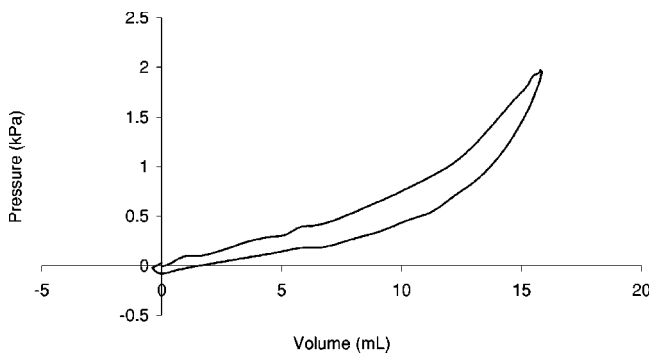


**Fig. 7 The dynamic pressure–volume relationship for the passively inflated heart, inflated with a period of 1.5 s**

of the estimated parameters as a percentage of the mean is tabulated in Table 1, which shows that with increasing levels of noise it is insufficient to use a single frame to estimate the constitutive parameters.

## Discussion

**Material Parameter Estimation.** A method for the characterization of soft tissue material properties has been developed based on FE modeling of MRI tissue tagged images. MR tissue tagging is used as a noninvasive method for accurate reconstruction of the 3D deformation field within the soft tissue structure. O'Dell et al. [33] have performed similar MR tagging experiments in isolated arrested dog hearts. They note that the regional wall thickness and geometry of the LV is an important factor in relation to the observed heterogeneity in passive strain. However, we are not aware of any previous report on the validation of material parameter estimation using this method.

We used displacement data in our objective function, in order to keep the error function as separate as possible from the model formulation. The use of strain in the error function would require a strain estimation, which in our implementation is derived from the model itself. We have an independent measure of the accuracy of the tracked tag data, but we do not have an independent measure of the accuracy of the reconstructed strains.

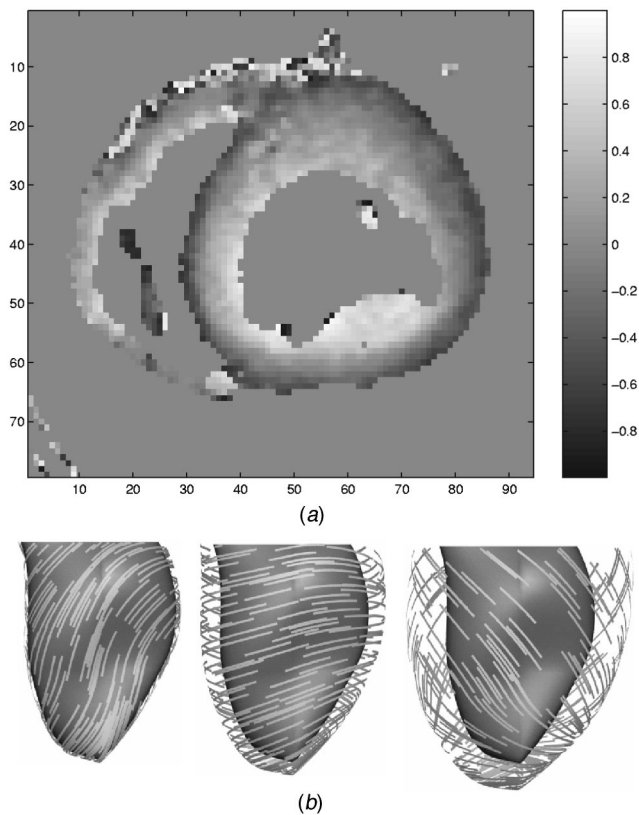


**Fig. 8** (a) Fiber angle (defined as the angle to the imaging plane) calculated from diffusion imaging. Gray is parallel to the image plane. The fitted fiber angles on the fitted LV geometry. A linear basis was used through the wall, and three different transmural locations are shown here, starting on the left the endocardial fibers (b), the midwall (c), and the epicardial fibers (d).

MR tissue tagging methods are limited by the relatively coarse resolution of tags (typically 5–7 mm). Recently, a number of novel methods have been proposed for high-resolution displacement [34,35], or velocity [36] mapping using MRI. These have the potential to reconstruct displacement at every pixel in the image and may allow the application of material parameter estimation to regional disease such as sub-transmural infarction. In addition, small animal hearts (e.g. mice) can be imaged using small-bore high field MR scanners [37], allowing material parameter estimation to be used in small animal disease models.

**Table 1** Standard deviations of material parameters in Monte-Carlo simulations with varying amounts of noise and numbers of frames included in the optimization

Noise (mm)	Frames	C1	b1	b2	b3
0.4	1	5%	4%	3%	4%
	3	1%	1%	1%	1%
	5	1%	1%	1%	1%
0.8	1	10%	7%	7%	13%
	3	1%	2%	1%	2%
	5	2%	2%	2%	3%
1.6	1	21%	16%	13%	22%
	3	4%	4%	7%	5%
	5	6%	4%	6%	8%
3.2	1	57%	28%	20%	43%
	3	15%	12%	14%	20%
	5	6%	5%	9%	9%

One advantage of this method over traditional material testing of small tissue specimens is that whole organs can be tested, avoiding the disruption of the tissue which often results from specimen preparation. Disadvantages of the technique include the need for repeatable cyclic deformation actuated within a MR scanner, the relatively complex geometries and tissue microstructure that must be modeled, and the relative lack of control of prescribed deformations. The latter two constraints require that a sophisticated FE solution procedure be adopted, which can model the material properties relative to the tissue microstructure. This technique allows for spatially varying material properties to be modeled and estimated, as in the current study. MRI can also be used to provide detailed information on the geometry via high-resolution 3D imaging methods, and tissue architecture via diffusion tensor imaging [8–12]. Recently, Tseng et al. [38] showed that it might also be possible to measure myocardial laminar sheet orientation from diffusion tensor imaging. This information could then be incorporated in micro-structurally based material laws [27].

**Gel Phantom Validation.** Validation of the method and apparatus using a deformable silicone gel phantom provided a good measure of the ability of the system to determine soft tissue material properties. The main aim of the gel phantom experiments was not to characterize the material behavior of the gel in detail, but to provide an independent measure of material properties in the case of a simple but realistic material law. Previously, the neo-Hookean law has been found to give a good approximation to the gel material behavior [4], and a similar gel phantom was used to validate the FE method of 3D displacement reconstruction from multi-slice MR tagged images [7]. The parameter estimation method was found to be unbiased (mean difference around 1%) and accurate (coefficient of variation of 9.8%).

The average estimate of the regionally varying gel material parameter was very close to the estimate of a constant parameter, as expected since the gel material properties should indeed be homogeneous. In the heart, we might expect some degree of regionally heterogeneity in the material properties, varying for instance from apex to base. In addition, regional disease such as myocardial infarction produces heterogeneous material properties around the heart. The ability to regionally vary material parameters, as demonstrated in the current study, will be useful in these applications.

**Isolated Heart Tests.** An experimental procedure was also devised and tested for the investigation of isolated heart preparations. In the absence of a homogeneous orthotropic material which can form MRI phantoms like the silicon gel used in this study, independent validation in the orthotropic case is not possible. However, the Monte-Carlo simulations in the case of the Guc-cione material law (Table 1) show that the parameters of this particular transversely isotropic material law can be accurately reconstructed from the MR data, dependent on the noise level and the number of frames included in the optimization. Of note is that it seems insufficient to characterize the material parameters for the high noise simulations using only a single frame, multiple frames are required this could simply be a matter of more data better defining the parameters or perhaps an increase in the range of available strains. The best form of material law for myocardium, and possible regional variations, are interesting topics for future study.

The parameters found are similar to those characterized by Guc-cione [23] in the study of inflated canine hearts. Although an exact correspondence was not necessarily expected due to differences in the experiment and modeling method, specifically this method is a data rich method which utilizes data from the entire heart resulting in a set of averaged parameters. Differences between species have been documented and also parameters have been found to vary regionally within the heart, specifically transmurally [40].

One novel aspect of our protocol was that the chordae tendonae linking the papillary muscles with the mitral valve were not cut

and we did not use a balloon inside the LV cavity. Many previous studies on isolated arrested hearts have included a flexible balloon inside the LV, but this may influence the resulting material properties and may impose surface tractions on the LV endocardial surface.

**Limitations and Future Work.** The reciprocating pump apparatus was sufficient for the volumes and cycle periods used in the current study, but is limited by the physical distance from the specimen to the pump imposed by the MR scanner. Thus, cycle frequencies of more than 0.8 Hz were not possible for stroke volumes greater than 60 mL. The compliance of the hose meant that the stroke volume and flow experienced in the scanner were somewhat different from that imposed at the pump. Minor changes in the apparatus (such as positioning the pump closer to the imaging area, or pneumatic valves close to the heart) will allow a greater range of volumes and frequencies. In addition, the reciprocating pump apparatus can also be used in studies investigating fluid mechanics problems, such as aortic flow, using velocity encoded MRI.

The choice of appropriate material law formulation for heart myocardium is currently an open research topic. Recently, Criscione et al. [28] have demonstrated that the classical expression of hyperelastic materials in terms of strain invariants is fundamentally ill posed in terms of parameter estimation. They propose alternative formulations based on strain attributes which are chosen to minimize the correlation between terms in the material law. Myocardial material laws based on this formulation show promise for material parameter estimation from MR displacement data, by reducing the correlation between fitted parameters (as found in the current study) and thereby improving the accuracy of the parameter estimation.

The ultimate aim of this work is to characterize the material properties of the heart in vivo. However, this will require the noninvasive estimation of LV filling pressure and other boundary conditions. In this case, the passive material properties could be determined from the late diastolic filling and atrial contraction.

The use of the isolated heart preparation to determine myocardial material parameters is not new [23]; however, MRI allows the noninvasive estimation of strain throughout the heart, and we hope that these methods can be extended to the in-vivo situation. One limitation with this method is that not all modes of deformation may be optimally present in the data, leading to under constrained parameters for some terms of the material law. Other experimental preparations may be better for the unique determination of all parameters [39].

The error function used penalized the error between the tracked and modeled data point positions. This is not the only possible formulation for example components of strain could be used to provide a measure of error that is not affected by rigid body transformation. We used displacement data because its accuracy has been independently validated.

## Conclusions

The apparatus and method developed in this study was capable of the accurate estimation of material parameters under controlled cyclical deformation conditions. Independent material tests and Monte Carlo simulations showed that the material parameters estimated were accurate and precise. Using this method, it will be possible to derive accurate estimates of regional soft tissue material properties in isolated heart preparations from MRI tissue tagged images.

## Acknowledgment

This work was supported by grants from Lotteries Health, NZ, Health Research Council of New Zealand, and the Foundation of Research Science and Technology, NZ. Dr. Pippa Storey implemented the diffusion tensor imaging pulse sequence. Dr. Gordon

Mallinson advised on the construction of the pump actuator. Dr. Bruce Smaill advised and assisted the animal experiments.

## References

- [1] Mandinovic, L., Eberli, F. R., Seiler, C., and Hess, O. M., 2000, "Diastolic Heart Failure," *Cardiovasc. Res.*, **45**, pp. 813–825.
- [2] Nielsen, P. M. F., Malcolm, D. T. K., Hunter, P. J., and Charette, P. G., 2002, "Instrumentation and Procedures for Estimating the Constitutive Parameters of Inhomogeneous Elastic Membranes," *Biomech. Modeling Mechanobiol.*, **1**, pp. 211–218.
- [3] Malcolm, D. T. K., Nielsen, P. M. F., Hunter, P. J., and Charette, P. G., 2002, "Strain Measurement in Biaxially Loaded Inhomogeneous Anisotropic Elastic Membranes," *Biomech. Modeling Mechanobiol.*, **1**, pp. 197–210.
- [4] Dokos, S., Le Grice, I. J., Smaill, B. H., Kar, J., and Young, A. A., 2000, "A Triaxial-Measurement Shear-Test Device for Soft Biological Tissues," *J. Biomech. Eng.*, **122**, pp. 471–478.
- [5] Zerhouni, E. A., Parish, D. M., Rogers, W. J., Yang, A., and Shapiro, E. P., 1988, "Human Heart: Tagging With MR Imaging—A Method for Noninvasive Assessment of Myocardial Motion," *Radiology*, **169**, pp. 59–63.
- [6] Axel, L., and Dougherty, L., 1989, "MR Imaging of Motion With Spatial Modulation of Magnetization," *Radiology*, **171**, pp. 841–845.
- [7] Young, A. A., Kraitchman, D. L., Dougherty, L., and Axel, L., 1995, "Tracking and Finite Element Analysis of Stripe Deformation in Magnetic Resonance Tagging," *IEEE Trans. Med. Imaging*, **14**, pp. 413–421.
- [8] Le Bihan, D., Mangin, J. F., Poupon, C., Clark, C. A., Pappata, S., Molko, N., and Chabriat, H., 2001, "Diffusion Tensor Imaging: Concepts and Applications," *J. Magn. Reson. Imaging*, **13**, pp. 534–546.
- [9] Basser, P. J., and Pierpaoli, C., 1998, "A Simplified Method to Measure the Diffusion Tensor From Seven MR Images," *Magn. Reson. Med.*, **39**, pp. 928–934.
- [10] Garrido, L., Wedeen, V. J., Kwong, K. K., Spencer, U. M., and Kantor, H., 1994, "Anisotropy of Water Diffusion in the Myocardium of Rat," *Circ. Res.*, **74**, pp. 789–793.
- [11] Hsu, E. W., Muzikant, A. L., Matulevicius, S. A., Penland, R. C., and Henriquez, C. S., 1998, "Magnetic Resonance Myocardial Fiber-Orientation Mapping With Direct Histological Correlation," *Am. J. Physiol.*, **274**, pp. H1627–H1634.
- [12] Scollan, D. F., Holmes, A., Winslow, R., and Forder, J., 1998, "Histological Validation of Myocardial Microstructure Obtained From Diffusion Tensor Magnetic Resonance Imaging," *Am. J. Physiol.*, **275**, pp. H2308–H2318.
- [13] Green, A. E., and Zerna, W., 1968, *Theoretical Elasticity*, 2nd ed., Oxford University Press, London.
- [14] Costa, K. D., Hunter, P. J., Rogers, J. M., Guccione, J. M., Waldman, L. K., and McCulloch, A. D., 1996, "A Three-Dimensional Finite Element Method for Large Elastic Deformations of Ventricular Myocardium: I—Cylindrical and Spherical Polar Coordinates," *J. Biomech. Eng.*, **118**, pp. 452–463.
- [15] Costa, K. D., Hunter, P. J., Wayne, J. S., Waldman, L. K., Guccione, J. M., and McCulloch, A. D., 1996, "A Three-Dimensional Finite Element Method for Large Elastic Deformations of Ventricular Myocardium: II—Prolate Spheroidal Coordinates," *J. Biomech. Eng.*, **118**, pp. 464–472.
- [16] Hunter, P. J., and Smaill, B. H., 1988, "The Analysis of Cardiac Function: A Continuum Approach," *Prog. Biophys. Mol. Biol.*, **52**, pp. 101–164.
- [17] Young, A. A., and Axel, L., 1992, "Three-Dimensional Motion and Deformation of the Heart Wall: Estimation With Spatial Modulation of Magnetization—A Model-Based Approach," *Radiology*, **185**, pp. 241–247.
- [18] Augenstein, K. F., McVeigh, E. R., and Young, A. A., 2001, "Magnetic Resonance Imaging and Ventricle Mechanics," *Philos. Trans. R. Soc. London*, **359**, pp. 1263–1275.
- [19] Young, A. A., Axel, L., Dougherty, L., Bogen, D. K., and Parenteau, C. S., 1993, "Validation of Tagging With MR Imaging to Estimate Material Deformation," *Radiology*, **188**, pp. 101–118.
- [20] Axel, L., Goncalves, R. C., and Bloomgarden, D., 1992, "Regional Heart Wall Motion: Two-Dimensional Analysis and Functional Imaging With MR Imaging," *Radiology*, **183**, pp. 745–750.
- [21] Young, A. A., Cowan, B. R., Thrupp, S. F., Hedley, W. J., and Dell'Italia, L. J., 2000, "Left Ventricular Mass and Volume: Fast Calculation With Guide-Point Modeling on MR Images," *Radiology*, **216**, pp. 597–602.
- [22] Choung, C. J., and Fung, Y. C., 1986, "Residual Stress in Arteries," pp. 117–129, In *Frontiers in Biomechanics*, G. W. Schmid-Schonbein, S. L.-Y. Woo, and B. W. Zweifach, eds., Springer-Verlag, New York.
- [23] Guccione, J. M., McCulloch, A. D., and Waldman, L. K., 1991, "Passive Material Properties of Intact Ventricular Myocardium Determined From a Cylindrical Model," *J. Biomech. Eng.*, **113**, pp. 42–55.
- [24] Omens, J. H., MacKenna, D. A., and McCulloch, A. D., 1993, "Measurement of Strain and Analysis of Stress in Resting Rat Left Ventricular Myocardium," *J. Biomech.*, **26**, pp. 665–676.
- [25] Hunter, P. J., Nielsen, P. M. F., Smaill, B. H., Le Grice, I. J., and Hunter, I. W., 1993, "An Anatomical Heart Model With Applications to Myocardial Activation and Ventricular Mechanics," in *High Performance Computing in Biomedical Research*, T. C. Pilkington, B. Loftis, S. L.-Y. Woo, T. C. Palmer, and T. F. Budinger, eds., CRC Press, Boca Raton, Florida, pp. 3–26.
- [26] Hunter, P. J., 1995, "Myocardial Constitutive Laws for Continuum Mechanics Models of the Heart," in *Advances in Experimental Medicine and Biology*, S. Sideman and R. Beyar, eds., Plenum Press, New York, Vol. 382, pp. 303–318.
- [27] Hunter, P. J., and Arts, T., 1997, "Tissue Remodelling With Micro-Structurally

- Based Material Laws,” in *Analytical and Quantitative Cardiology: From Genetics to Function*, S. Sideman and R. Beyar, eds., Plenum Press, New York, pp. 215–225.
- [28] Criscione, J. C., McCulloch, A. D., and Hunter, W. C., 2002, “Constitutive Framework Optimized for Myocardium and Other High-Strain, Laminar Materials With One Fiber Family,” *J. Mech. Phys. Solids*, **50**, pp. 1681–1702.
- [29] www.cmiss.org
- [30] Gill, P. E., Murray, W., and Wright, M. H., *Practical Optimization*, Academic Press, London.
- [31] Young, A. A., “Model Tags: Direct Three-Dimensional Tracking of Heart Wall Motion From Tagged Magnetic Resonance Images,” *Med. Image Anal.*, **3**, pp. 361–372.
- [32] Atalar, E., and McVeigh, E. R., 1994, “Optimization of Tag Thickness for Measuring Position With Magnetic Resonance Imaging,” *IEEE Trans. Med. Imaging*, **13**, pp. 152–160.
- [33] O’Dell, W., 1995, “Myocardial Deformation Analysis in the Passive Dog Heart Using High Resolution MRI Tagging,” Ph.D. thesis, Dept. of Biomedical Engineering, Johns Hopkins Univ.
- [34] Aletras, A. H., and Wen, H., 2001, “Mixed Echo Train Acquisition Displacement Encoding With Stimulated Echoes: An Optimized DENSE Method for In Vivo Functional Imaging of the Human Heart,” *Magn. Reson. Med.*, **46**, pp. 523–534.
- [35] Osman, N. F., McVeigh, E. R., and Prince, J. L., 2000, “Imaging Heart Motion Using Harmonic Phase MRI,” *IEEE Trans. Med. Imaging*, **19**, pp. 186–202.
- [36] Zhu, Y., 1999, “A Spatiotemporal Model of Cyclic Kinematics and Its Application to Analyzing Nonrigid Motion With MR Velocity Images,” *IEEE Trans. Med. Imaging*, **18**, pp. 557–569.
- [37] Epstein, F. H., Yang, Z. Q., Gilson, W. D., Berr, S. S., Kramer, C. M., and French, B. A., 2002, “MR Tagging Early After Myocardial Infarction in Mice Demonstrates Contractile Dysfunction in Adjacent and Remote Regions,” *Magn. Reson. Med.*, **48**, pp. 399–403.
- [38] Tseng, W.-Y. I., Wedeen, V. J., Reese, T. G., Smith, R. N., and Halpern, E. H., 2003, “Diffusion Tensor MRI of Myocardial Fibers and Sheets: Correspondence With Visible Cut-Face Texture,” *J. Magn. Reson. Imaging*, **17**, pp. 31–42.
- [39] Humphrey, J. D., 2002, *Cardiovascular Solid Mechanics: Cells, Tissues, and Organs*, Springer-Verlag, New York.
- [40] Costa, K. D., Holmes, J. W., and McCulloch, A. D., 2001, “Modelling Cardiac Mechanical Properties in Three Dimensions,” *Philos. Trans. R. Soc. London*, **359**, pp. 1233–1250.